Editors' Suggestion

Accurate Determination of Hubble Attenuation and Amplification in Expanding and Contracting Cold-Atom Universes

S. Banik,[1] M. Gutierrez Galan,[1] H. Sosa-Martinez,[1] M. Anderson,[1] S. Eckel,[2] I. B. Spielman,[1] and G. K. Campbell[1]

[1]*Joint Quantum Institute, National Institute of Standards and Technology, and University of Maryland, College Park, Maryland 20742, USA*

[2]*Sensor Sciences Division, National Institute of Standards and Technology, and University of Maryland, Gaithersburg, Maryland 20899, USA*

(Received 19 July 2021; revised 16 November 2021; accepted 7 February 2022; published 28 February 2022)

In the expanding universe, relativistic scalar fields are thought to be attenuated by "Hubble friction," which results from the dilation of the underlying spacetime metric. By contrast, in a contracting universe this pseudofriction would lead to amplification. Here, we experimentally measure, with fivefold better accuracy, both Hubble attenuation and amplification in expanding and contracting toroidally shaped Bose-Einstein condensates, in which phonons are analogous to cosmological scalar fields. We find that the observed attenuation or amplification depends on the temporal phase of the phonon field, which is only possible for nonadiabatic dynamics. The measured strength of the Hubble friction disagrees with recent theory [Gomez Llorente *et al.*, Phys. Rev. A **100**, 043613 (2019) and Eckel *et al.*, SciPost Phys. **10**, 64 (2021)].

DOI: 10.1103/PhysRevLett.128.090401

During the early universe's rapid expansion, primordially fluctuating scalar fields are thought to have been exponentially redshifted and attenuated by the expanding spacetime metric, where "Hubble friction" contributes to the latter [1]. Unlike true friction, Hubble friction is nondissipative and therefore, while it attenuates scalar fields in an expanding universe, it would amplify them in a contracting universe. In previous work [2], our group showed that an atomic Bose-Einstein condensate (BEC) in an expanding toroidal trap could simulate elements of an expanding universe, including the redshifting of phonons in analogy to the redshifting of photons. Here, we build upon these studies by including contracting universes; measuring both Hubble attenuation and amplification with fivefold increased precision; and showing that the magnitude of Hubble friction disagrees with recent theoretical work [3,4].

While the study of astrophysical systems is ordinarily limited to observations, the development of well-controlled laboratory systems has enabled tabletop realizations of general relativistic phenomena. Examples from a variety of physical platforms ranging from classical fluids to cold atomic systems include: the realization of acoustic black hole horizons [5–7]; stimulated and spontaneous Hawking radiation [8–10]; and scattering processes around rotating black holes [11]. With their unprecedented control and measurement capabilities, ultracold atoms are an emerging platform for realizing minimal models relevant to high energy physics [12], astrophysics [13–16], and cosmology [2,17–19].

In BECs, phonons are scalar fields that evolve approximately according to an effective spacetime metric defined by the background BEC [18]. For toroidally shaped BECs, expanding or contracting 1D universes can be simulated by dynamically changing the BEC's radius and observing the evolution of azimuthal phonons. Unlike the expansion observed in the photon-dominated epoch of the universe, we explore nonadiabatic expansions and contractions where the rate of the metric change exceeds the oscillation frequency.

Phonons are predominately phase excitations with respect to the BEC's order parameter. For a toroidal BEC with radius $R(t)$ (see Fig. 1) and 3D volume $\mathcal{V}(t)$, azimuthal phonons with mode number m, have an approximate phase profile $\delta\phi_{1D}(\theta, t) \equiv \delta\phi(t)\sin(m\theta)$ independent of r and z and obey the wave equation [4]

$$\left\{\partial_t^2 + \left[2\gamma + \frac{\dot{\mathcal{V}}(t)}{\mathcal{V}(t)}\right]\partial_t + \omega_m^2(t)\right\}\delta\phi(t) = 0 \qquad (1)$$

at low energy (i.e., small m). Here, the instantaneous angular frequency is $\omega_m = mc_\theta(t)/R(t)$, for speed of sound $c_\theta(t)$. Because we focus exclusively on the $m = 1$ mode, the m subscript is omitted in what follows. The quantity in square brackets is reminiscent of damping because it multiplies the first derivative of time. It includes a phenomenological damping constant γ [20] and the nondissipative Hubble friction $\dot{\mathcal{V}}/\mathcal{V}$ arising from the changing metric defined by the background condensate. We model the external potential

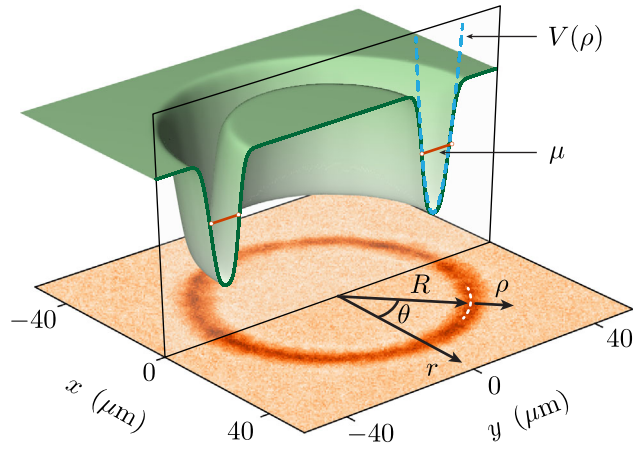

FIG. 1. Ring-trapping potential and resulting atomic density. The green surface schematically depicts the trapping potential; the orange lines mark the typical chemical potential μ. The blue-dashed curve shows a power law fit to the potential (up to μ) around $\rho = |r - R| = 0$ giving exponent 2.02(3) for this example. The measured 2D density $n_{2D}(\rho, \theta)$ is shown in the $\mathbf{e}_x$-$\mathbf{e}_y$ plane (with peak density 165 μm^{-2}) and the white dashed arc marks the mean radius R. Because of the short 500 μs TOF, the observed width of the ring is slightly in excess of that anticipated from the *in situ* TF approximation.

(see Fig. 1) as quadratic in z and power law in $\rho = |r - R|$; in the Thomas-Fermi (TF) and thin-ring approximations, these lead to the BEC's 3D volume $\mathcal{V} \propto R^{\alpha}$ and $c_\theta \propto R^{-\alpha/2}$, where the value of the constant α depends on the potential [4]. Rather than detecting $\delta\phi_{1D}$, we measure the associated density perturbation $\delta n_{1D}(\theta, t) = \delta n(t) \sin(m\theta)$. The relationship between $\delta\phi$ and δn is $\partial_t \delta\phi = -(g/\hbar)(\delta n / R^{\alpha})$, in terms of the Gross-Pitaevskii equation [22] interaction constant g.

In our experiments, the potential $V(\rho)$ is nominally fixed during expansion or contraction, predicting $\dot{\mathcal{V}}/\mathcal{V} = \gamma_H \dot{R}/R$ with strength $\gamma_H = \alpha$. In expanding systems ($\dot{R} > 0$) the Hubble friction term attenuates phonons, while in contracting systems it amplifies them. In the nonadiabatic regime $\dot{R}/R \gtrsim \omega_m$, the timing of expansion or contraction relative to the phonon's temporal phase becomes important for subsequent dynamics. Because the Hubble friction term includes the product of $\dot{R}/R$ and $\delta n(t) \propto \partial_t \delta\phi(t)$, tuning the timing of expansion or contraction relative to the oscillation changes the degree of amplification or attenuation.

Our experiments [23,24] begin with quasi-2D ^{23}Na BECs with $N \approx 1 \times 10^5$ atoms confined in a pair of blue-detuned ($\lambda = 532$ nm) optical dipole traps. The chemical potential is $\mu \approx h \times 2.7$ kHz. Harmonic vertical confinement, with frequency $\omega_z/2\pi \approx 1.2$ kHz, is provided by a horizontally propagating Hermite-Gauss TEM$_{01}$ beam. We generate nearly arbitrary space and time-dependent potentials in the $r - \theta$ plane by imaging $\lambda = 532$ nm laser light reflected by a digital micromirror device (DMD) onto the BEC. We use these potentials to create toroidal traps with variable radius R (see Fig. 1) and projected radial width ≈ 5 μm.

Anearly pure [94(2)%] azimuthal phonon excitation with mode number $m = 1$ is generated by perturbing the toroidal BEC with a potential $V_{ph} \sin(m\theta)$ [25]. This repulsive potential—generated by the DMD—is applied for 2 ms, imprinting the phonon's phase modulation onto the BEC. After imprinting, the phonon evolves for an initial time t_i, at which point the torus is expanded or contracted using an error function profile [2], with 10%–90% rise time 3.6 ms, and continues to evolve for up to ≈ 150 ms. For expansion, the initial and final radii are $R_i = 11.9(2)$ μm

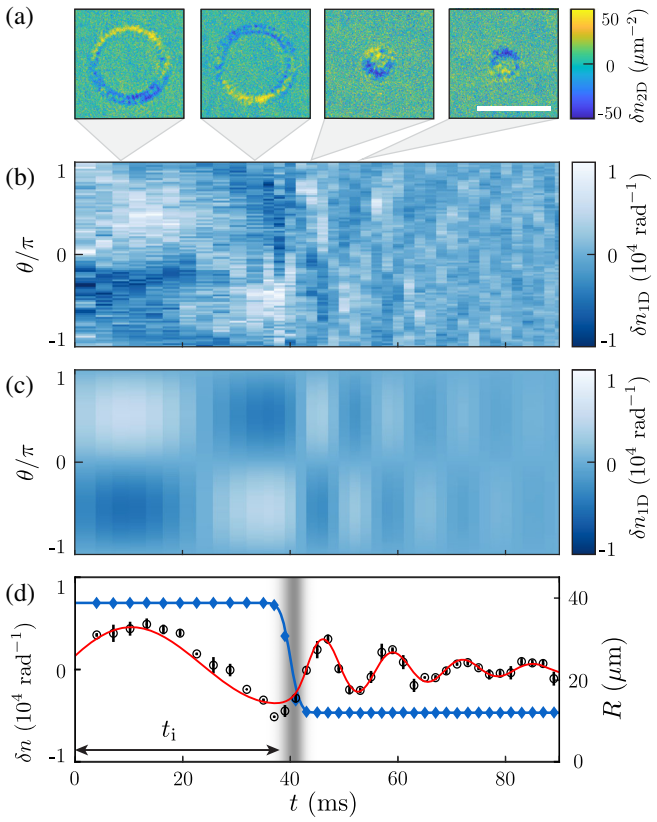

FIG. 2. Phonon evolution in a contracting toroidally shaped BEC, averaged over three measurements. (a) Density perturbations for a ring with $R_i = 38.4(6)$ μm at 10 ms and 35 ms, and $R_f = 11.9(2)$ μm at 45 ms and 53 ms. The density scale of images before contraction is multiplied by 2. The horizontal bar corresponds to 80 μm. (b) Experimental measurements and (c) fit to Eq. (1) of angular density perturbation δn_{1D} as a function of azimuthal angle θ and time t, where the ring contraction occurs at t_i. (d) Phonon amplitude δn as a function of time. The circles plot the phonon amplitude obtained from fitting each time slice of (b) to a sinusoid [26]. The red curve is the instantaneous amplitude from the fit in (c). The diamonds are the measured BEC mean radius and the blue line is the programmed radius. The grayscale bar encodes the value of $|\dot{R}/R|$, with a maximum of 328(11) s^{-1} at $t_{peak} = 41$ ms. The arrow indicates $t_i = 38.2$ ms.

and $R_f = 38.4(6)$ μm; these are reversed for contraction [26]. We detect the phonon at various points during the complete evolution using partial transfer absorption imaging [27] after a short 500 μs time of flight, giving the 2D density $n_{2D}(\rho, \theta)$ [see Fig. 1].

The phonon excitation's density perturbation [see Fig. 2(a)] is $\delta n_{2D} = n_{2D} - n^0_{2D}$, where n^0_{2D} is the density with no phonon present. Integrating along r gives the azimuthal density perturbation $\delta n_{1D}(\theta, t)$. Figure 2(b) shows the time evolution of δn_{1D}, and Fig. 2(c) shows the resulting fit to Eq. (1), from which we obtain both the redshift or blueshift (via c_θ) and the Hubble friction (from γ_H). In our system, the phenomenological damping γ is observed to depend strongly on radius. Instead, we parameterize the damping in terms of the quality factor $Q = \omega/2\gamma$, which is more independent of radius than γ (see [24,28]).

Because the 3.6 ms expansion or contraction is a small fraction of the phonon oscillation period, the overall fit is insensitive to how Q interpolates between Q_i to Q_f. We therefore assume a simple linear dependence of Q on R. As shown in Fig. 2(b), our data typically has less than one oscillation before R changes; to reduce the uncertainty in Q_i and $\omega(R_i)$, we include fixed-radius rings in a simultaneous fit. These fits include as free parameters γ_H, Q_i, Q_f, and α as well as the initial speed of sound $c_{\theta,i}$, initial amplitude δn_i, initial temporal phase φ_0, and an overall offset angle $\delta\theta$ capturing a small angular misalignment between the camera and DMD. $c_\theta(t) = c_{\theta,i}(R(t)/R_i)^{-\alpha/2}$ follows the expected scaling.

Figure 2(d) summarizes the outcome of this fit. The red curve is the time-dependent density perturbation δn obtained from the full fit, while the circles plot δn from independent fits to $\delta n \sin(\theta + \delta\theta)$ of each time slice in Fig. 2(b), providing a 1D representation of the data in Fig. 2(b). The blue curve displays the radius of the DMD pattern while the diamonds plot R obtained from a 2D TF fit to the observed density distribution [29]. The gray band plots $\dot{R}/R$ during contraction, with maximum $\dot{R}/R \approx 1.53 \times \omega$.

We study the hypothesized impact of the phonon phase on the Hubble friction during expansion or contraction by changing t_i [see Fig. 2(d)], thereby phase-shifting the phonon by $(c_{\theta,i}/R_i)t_i$. We define t_{peak} as the time when the Hubble friction reaches its peak strength, i.e., when $|\dot{R}/R|$ is maximal. The phase of the phonon at t_{peak} is $\varphi_{\text{peak}} \equiv \int_0^{t_{\text{peak}}} dt\omega(t) + \varphi_0$. Figure 3 shows example time-traces with multiple t_i for both expansion and contraction, providing a complete picture to investigate the strength of Hubble friction. The black circles show the time evolution of the phonon amplitude $\delta n(t)$ for a range of t_i for both expansions (a) and contractions (b).

The red curves in Fig. 3 show the results of global fits [30] of Eq. (1) to our complete dataset, which includes

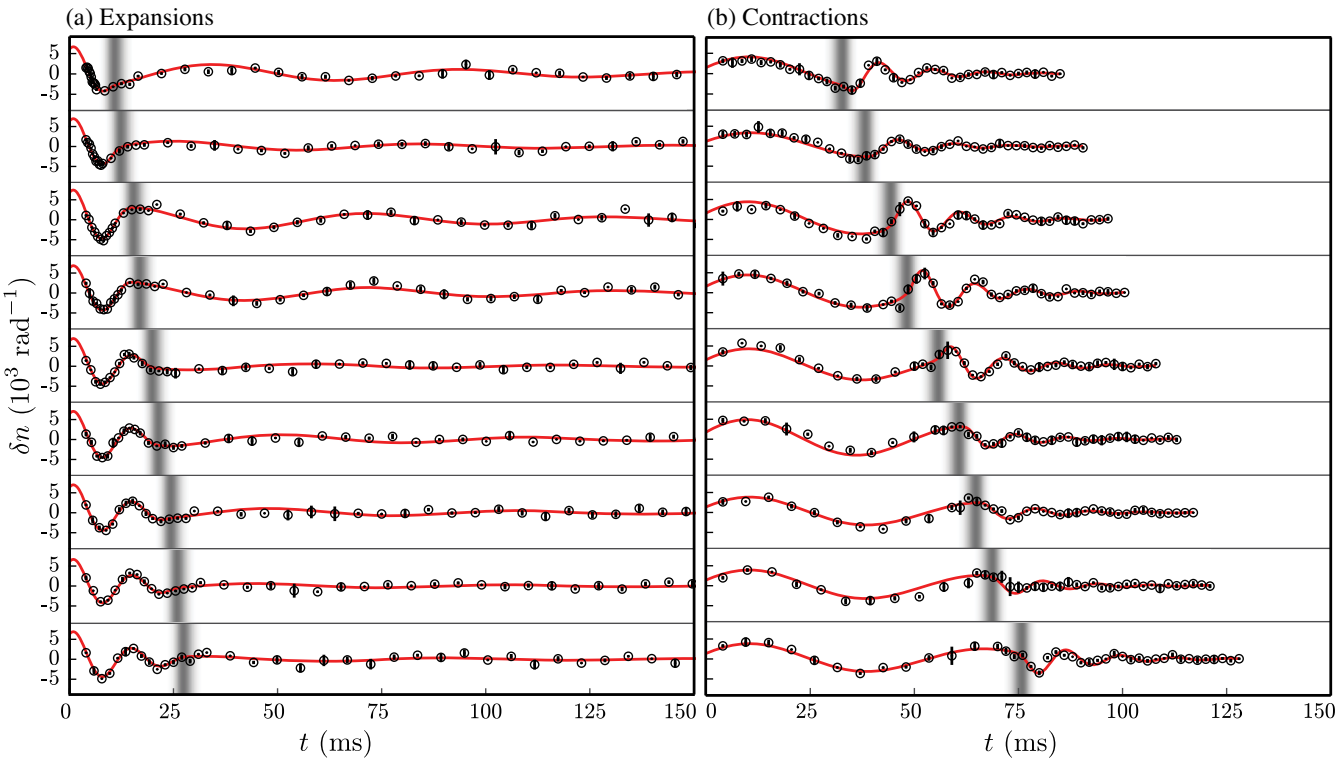

FIG. 3. Phonon amplitude δn as a function of time t for (a) expanding and (b) contracting tori. The symbols, curves, and grayscale bars are all as notated in Fig. 2(d). The expansion data (a) used $R_i = 11.9(2)$ μm and $R_f = 38.4(6)$ μm, and vice versa for contraction (b). The red curves show simultaneous fits to a complete dataset, which includes all expansions or contractions.

17 contractions and 11 expansions. The parameters γ_H, α, Q_i, Q_f, $c_{\theta,i}$, and δn_i are global, i.e., they are shared across all time traces. For each time trace, δn_i is scaled by the atom number $N(t)$ for that trace, and $c_{\theta,i}$ is correspondingly scaled by $\propto N(t)^{\alpha/2}$ [31]; this accounts for both atom loss during and after expansion or contraction and for overall drifts in atom number during data acquisition. Each global fit includes seven additional time traces, each with constant R, roughly from R_i to R_f. Because $c_\theta(R) \propto R^{\alpha/2}$ in stationary rings, these additional datasets further constrain α. We performed separate global fits for expansion and contraction data, giving an independent measure of their Hubble friction coefficients. Finally, to mitigate potential systematic biases introduced by overfitting, we perform these global fits in eight different ways, with the number of fit parameters varying between 32 and 101 for $\approx 7.5 \times 10^4$ independent data points. Each fit yields different best-fit values, but generally they agree within 2-σ. These fitting methods differ on whether the temporal and azimuthal phases are shared across the time traces and if atom number varies within each time trace (see Supplemental Material [32] for details). We take the mean of the values obtained from the eight methods as the best fit value. Their standard deviation is added in quadrature to the average 1-σ uncertainty from the fit to obtain the final uncertainty in the measurement.

Table I lists the best-fit values, with γ_H different for contraction and expansion. The values of α are in agreement with each other. For our power-law potential model [4], α ranges from 1/2 (for a harmonic potential) to 1 (for a hard-wall potential). Our average value of $\alpha \approx 0.495$ suggests that we have a harmonic potential in both z and r. The values of $c_{\theta,i}$ and δn_i depend on the initial density, which is larger for expansions (i.e., smaller initial rings) than contractions.

Lastly, we confirm our expectation that the phonon phase φ_{peak} has a marked impact on the amplitude following expansion or contraction in the nonadiabatic limit. Our experiments probe $1.3 \lesssim \varphi_{\text{peak}}/\pi \lesssim 2.9$. Figure 4(a) illustrates our process for obtaining the final amplitudes A_f where we fit the oscillatory behavior to an exponentially decaying sinusoid with the amplitude and temporal phase as free parameters. By contrast, the initial amplitude A_i is obtained from our global fit, from the envelope of the decaying sinusoid evaluated at t_{peak}. Figure 4(b) plots the fractional change in amplitude A_f/A_i versus φ_{peak} with black circles, and the solid blue curve depicts A_f obtained from our global fits. Our simulations (grey curves) show that the significant oscillations for $\gamma_H = 0$, give way to more uniform gain with increasing γ_H. The measured values of A_f/A_i are generally larger than would be expected for $\gamma_H = 0$, showing Hubble amplification due to contraction. Unlike Ref. [2], which probed $1.8 \lesssim \varphi_{\text{peak}}/\pi \lesssim 2.1$, where A_f/A_i has little dependence on Hubble friction, our greater range of φ_{peak} allows us to better constrain γ_H. In addition to the overall oscillation, an additional dependence on ϕ_{peak} appears and is not captured by our model (data below $\phi_{\text{peak}}/\pi < 2$ generally lie above the $\gamma_H = 0.36$ curve, and below for $\phi_{\text{peak}}/\pi > 2$). This additional dependence may indicate a more complicated damping process for our phonons that could obscure our fitting for γ_H.

The observed oscillatory dependence of A_f on φ_{peak} results from the rapid nonadiabatic, i.e., superluminal, contraction in this experiment. The solid red curve emphasizes this point by plotting the simulated behavior for a

TABLE I. Best fit global parameters.

	Q_i	Q_f	α	γ_H	$c_{\theta,i}$ (mm/s)	δn_i (rad^{-1})
Expansion	3.5(1)	4.4(2)	0.47(1)	0.28(4)	5.42(2)	7.47(13)
Contraction	7.8(3)	3.5(1)	0.52(3)	0.36(3)	4.36(4)	4.50(5)

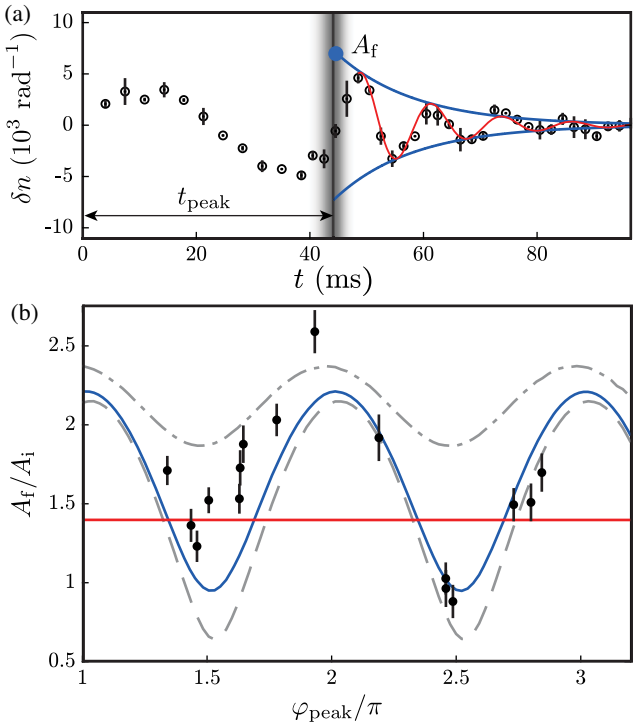

FIG. 4. Phonon amplitude vs phase. (a) Data (black circles), fit (red curve), and oscillation envelope (blue curve) used to extract the amplitude A_f at t_{peak}. The grayscale bar is as notated in Fig. 2(d). (b) Ratio of amplitudes A_f/A_i versus φ_{peak}, the oscillation's phase at t_{peak}. The black circles plot the data, and the error bars correspond to the fit uncertainty in the determination of A_f. The gray dashed, blue solid, and gray dashed-dot curves show the prediction of Eq. (1) for $\gamma_H = 0$, 0.36, and 1, respectively, with $\alpha = 0.52$. The red line indicates the prediction for an adiabatic contraction.

slow adiabatic contraction, computed with $\gamma = 0$. No dependence on φ_{peak} is present in this limit, as the phonon would undergo many oscillations during expansion and therefore lose any dependence on initial phase. The deviation from the adiabatic curve is associated with "classical" stimulated emission or absorption (described by the mean field Gross-Pitaevskii equation) into or out of the phonon field, in much the same way that these processes have been observed in acoustic black holes [14].

Our data generally agree with the predictions of Refs. [3,4], with the notable exception $\gamma_H \neq \alpha$. This discrepancy could be due to three possible effects. First, the simple scaling of c_θ with R holds only in the thin-ring approximation, and this can cause up to a 10% error in α. Second, while the excitation of higher azimuthal modes should have little impact (due to angular momentum conservation), expansion or contraction-driven mode mixing with higher excited radial modes (from nonadiabatic expansion) can contribute to an error in γ_H, which we estimate may be as high as 20%. Third, we create large-amplitude phonons to maximize our detection signal, and this may lead to nonlinear damping effects [35]. We note that general relativity is itself a nonlinear wave equation, so related effects are potentially present in true cosmology. In this linear regime, this complicates our measurement of γ_H, and potentially causes the additional dependence on ϕ_{peak} seen in Fig. 4(b).

For future experiments, our system is flexible enough to explore different metric scalings such as 2D expansions or contractions where $\gamma_H > 1$, as suggested in Ref. [4]. Our experimental setup could also readily explore other analogue gravity systems such as black hole horizons in 2D systems, where, for example the acoustic metric resulting from quantized vortices could open new directions [36].

The authors are grateful to T. Jacobson for useful discussions and to S. Mukherjee and M. Doris for a careful reading of the manuscript. This work was partially supported by NIST and NSF through the Physics Frontier Center at the Joint Quantum Institute.

[1] D. Baumann, in *Physics of the Large and the Small* (World Scientific, Singapore, 2011), pp. 523–686.
[2] S. Eckel, A. Kumar, T. Jacobson, I. B. Spielman, and G. K. Campbell, Phys. Rev. X **8**, 021021 (2018).
[3] J. M. Gomez Llorente and J. Plata, Phys. Rev. A **100**, 043613 (2019).
[4] S. Eckel and T. Jacobson, SciPost Phys. **10**, 64 (2021).
[5] G. Rousseaux, C. Mathis, P. Maïssa, T. G. Philbin, and U. Leonhardt, New J. Phys. **10**, 053015 (2008).
[6] T. G. Philbin, C. Kuklewicz, S. Robertson, S. Hill, F. König1, and U. Leonhardt, Science **319**, 1367 (2008).
[7] H. S. Nguyen, D. Gerace, I. Carusotto, D. Sanvitto, E. Galopin, A. Lemaître, I. Sagnes, J. Bloch, and A. Amo, Phys. Rev. Lett. **114**, 036402 (2015).
[8] F. Belgiorno, S. L. Cacciatori, M. Clerici, V. Gorini, G. Ortenzi, L. Rizzi, E. Rubino, V. G. Sala, and D. Faccio, Phys. Rev. Lett. **105**, 203901 (2010).
[9] E. Rubino, J. McLenaghan, S. C. Kehr, F. Belgiorno, D. Townsend, S. Rohr, C. E. Kuklewicz, U. Leonhardt, F. König, and D. Faccio, Phys. Rev. Lett. **108**, 253901 (2012).
[10] J. Steinhauer, Nat. Phys. **12**, 959 (2016).
[11] T. Torres, S. Patrick, A. Coutant, M. Richartz, E. W. Tedford, and S. Weinfurtner, Nat. Phys. **13**, 833 (2017).
[12] C. Cao, E. Elliott, J. Joseph, H. Wu, J. Petricka, T. Schäfer, and J. E. Thomas, Science **331**, 58 (2011).
[13] W. G. Unruh, Phys. Rev. Lett. **46**, 1351 (1981).
[14] J. Steinhauer, Nat. Phys. **10**, 864 (2014).
[15] Y. Ohashi, H. Tajima, and P. van Wyk, Prog. Part. Nucl. Phys. **111**, 103739 (2020).
[16] V. I. Kolobov, K. Golubkov, J. R. Muñoz de Nova, and J. Steinhauer, Nat. Phys. **17**, 362 (2021).
[17] L. J. Garay, J. R. Anglin, J. I. Cirac, and P. Zoller, Phys. Rev. Lett. **85**, 4643 (2000).
[18] C. Barceló, S. Liberati, and M. Visser, Phys. Rev. A **68**, 053613 (2003).
[19] U. R. Fischer and R. Schützhold, Phys. Rev. A **70**, 063615 (2004).
[20] This phenomenological damping term can account for Landau and Beliaev damping mechanisms [21] as well as imperfections in the confining potential.
[21] M.-C. Chung and A. B. Bhattacherjee, New J. Phys. **11**, 123012 (2009).
[22] F. Dalfovo, S. Giorgini, L. P. Pitaevskii, and S. Stringari, Rev. Mod. Phys. **71**, 463 (1999).
[23] Y.-J. Lin, A. R. Perry, R. L. Compton, I. B. Spielman, and J. V. Porto, Phys. Rev. A **79**, 063631 (2009).
[24] A. Kumar, N. Anderson, W. D. Phillips, S. Eckel, G. K. Campbell, and S. Stringari, New J. Phys. **18**, 025001 (2016).
[25] V_{ph} is set to 0.8 times the overall potential depth.
[26] Unless stated otherwise, all uncertainties on numerical quantities are the uncorrelated combination of 1-σ statistical and systematic uncertainties, while uncertainty bars in the figures include only the statistical contribution.
[27] A. Ramanathan, S. R. Muniz, K. C. Wright, R. P. Anderson, W. D. Phillips, K. Helmerson, and G. K. Campbell, Rev. Sci. Instrum. **83**, 083119 (2012).
[28] G. E. Marti, R. Olf, and D. M. Stamper-Kurn, Phys. Rev. A **91**, 013602 (2015).
[29] By contrast with Ref. [2], the BEC follows the contraction profile without overshoot or oscillation because of tighter radial confinement.
[30] Joint-Quantum-Institute, Data and analysis codes for the hubble friction experiment, https://github.com/JQIamo/hubFrct_2021 (2021).
[31] This can be derived from Eq. (4.8) and Eq. (4.20) of [4].

[32] See Supplemental Material at http://link.aps.org/supplemental/10.1103/PhysRevLett.128.090401 for data and data analysis codes for the experiment, which includes Refs. [33,34].
[33] J. Jarvis, C. Judice, and W. Ninke, Comput. Graph. Image Proc. **5**, 13 (1976).
[34] E. M. Seroka, A. V. Curiel, D. Trypogeorgos, N. Lundblad, and I. B. Spielman, Opt. Express **27**, 36611 (2019).
[35] N. Katz, J. Steinhauer, R. Ozeri, and N. Davidson, Phys. Rev. Lett. **89**, 220401 (2002).
[36] A. Coutant and S. Weinfurtner, arXiv:1504.00691.